# Neutron Reflectivity Characterization of the Photoacid Reaction–Diffusion Latent and Developed Images of Molecular Resists for Extreme Ultraviolet Lithography

**7 AUTHORS**, INCLUDING:

Wen-Li Wu
National Institute of Standards and Technology
**239** PUBLICATIONS   **3,021** CITATIONS

SEE PROFILE

Christopher K Ober
Cornell University
**587** PUBLICATIONS   **15,885** CITATIONS

SEE PROFILE

# Neutron Reflectivity Characterization of the Photoacid Reaction-Diffusion Latent and Developed Images of Molecular Resists for Extreme Ultraviolet Lithography

Vivek M. Prabhu,*,[†] Shuhui Kang,[†] Jing Sha,[§] Peter V. Bonnesen,[⊥] Sushil Satija,[‡] Wen-li Wu,[†] and Christopher K. Ober[§]

[†]Polymers Division and [‡]Center for Neutron Research, National Institute of Standards & Technology, Gaithersburg, Maryland 20899, United States

[§]Materials Science & Engineering, Cornell University, Ithaca, New York 14853, United States

[⊥]Center for Nanophase Materials Sciences, Oak Ridge National Laboratory, Oak Ridge, Tennessee 37831, United States

**ⓢ** *Supporting Information*

**ABSTRACT:** Lithographic feature size requirements have approached a few radius of gyration of photoresist polymers used in thin-film patterning. Furthermore, the feature dimensions are commensurate with the photoacid diffusion length that defines the underlying latent image. Smaller imaging building blocks may enable reduced feature sizes; however, resolution limits are also dependent upon the spatial extent of the photoacid-catalyzed reaction diffusion front and subsequent dissolution mechanism. The reaction-diffusion front was characterized by neutron reflectivity for ccc stereoisomer-purified, deuterium-labeled *tert*-butoxycarbonyloxy calix[4]resorcinarene molecular resists. The spatial extent of the reaction front exceeds the size of the molecular resist with an effective diffusion constant of $(0.13 \pm 0.06)$ nm$^2$/s for reaction times longer than 60 s, with the maximum at shorter times. Comparison to a mean-field reaction-diffusion model shows that a photoacid trapping process provides bounds to the spatial and extent of reaction via a reaction-limited mechanism whereas the ratio of the reaction rate to trapping rate constants recovers the effective diffusion peak. Under the ideal step-exposure conditions, surface roughness was observed after either positive- or negative-tone development. However, negative-tone development follows a surface-restructuring mechanism rather than etch-like dissolution in positive-tone development.
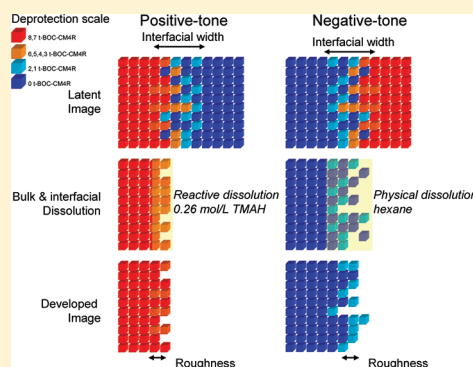
## 1. INTRODUCTION

Since the invention of chemically amplified photoresists,[1,2] features of increased resolution continue to meet rapid manufacturing demands.[3] However, strategies to extend critical dimension (CD) feature sizes below 22 nm by double patterning with 193 nm immersion deep-ultraviolet (UV) lithography and below 16 nm with extreme-ultraviolet (EUV) lithography require continued improvements to photoresists as the CD approaches a few radius of gyration ($R_g$) of the photoresist polymers. Chemically amplified photoresists are formulations of an acid-sensitive polymer blended with photoacid generators (PAGs) and other additives. Photolysis (by EUV or UV light) of the molecularly mixed PAG within the thin film forms photoacids that diffuse and catalyze a reaction of acid-sensitive protecting groups during a postexposure bake (PEB) step forming a latent image. This deprotection process increases the solubility of the polymer resist in a positive-tone developer solution.

The fidelity of the final patterned structure depends upon the interfacial structure formed by the reaction diffusion of photoacids into unexposed regions that induces image blurring.[4–7] Controlling the photoacid reaction-diffusion process remains a strategy to achieve higher-resolution resists with low line-edge roughness.[2] In this case, the interface between exposed and unexposed photoresists is of direct interest. Model interfaces provide a route to applying high-resolution experimental methods to probe these fundamentals. Houle et al. expose a photoresist thin film to a highly absorbing UV wavelength such that only the surface is exposed, not the entire film.[8–10] Therefore, subsequent PEB processing has characteristics of a 1D photoacid diffusion gradient in this in-situ-formed photoacid layer. This approach has the advantage that the photoacid diffuses within one resist media and the reaction-diffusion kinetics may be quantified by combining Fourier transform infrared spectroscopy (FTIR) with stochastic modeling. Lin et al. used a bilayer strategy by placing PAG in the top layer of a bilayer thin film that can be flood UV exposed (PEB) and developed.[11,12] This model interface was prepared by successive spin coating of a photoresist film and a second polymer film containing PAG (in a nonsolvent for the first film) to form a bilayer that mimics the lithographic line by rotating

the line edge rather than the vertical edge to form a planar interface. This provides a sharp initial photoacid step profile after exposure because the photoacid is only in the top layer. This approach was used to measure the deprotection profile with high-resolution neutron reflectivity after the photoacid diffused and deprotected deuterium-labeled poly(*tert*-butoxy-carbonyloxystyrene) (PBOCSt) resists applicable to 248 nm lithography.[11] This methodology was applied to several other polymer resist systems, including poly(methyladamantyl methacrylate) resists at 193 nm[13,14] and deuterium-labeled poly(*tert*-butyl acrylate-*co*-hydroxystyrene) resists for EUV lithography,[15] demonstrating neutron reflectivity methods[16] as a strategy to providing nanometer-resolution insight into the photoacid diffusion mechanism in polymer resists.

Molecular resists are alternatives to polymers with a smaller $R_g$ to enable reduced line-edge roughness and achieve smaller CD. Because of the smaller size, entropy of mixing arguments favor intimately mixed PAG and molecular resist blends.[17,18] Also, molecular resists are free of intermolecular entanglement typical in polymers that swell during the dissolution/development processes. Despite these advantages, as long as the photoacid remains free to diffuse during the PEB, the CD becomes photoacid-diffusion-length ($L_d$)-limited, rather than pixel-size- or $R_g$-limited. Kang et al. studied molecular resists using an improved bilayer preparation via a poly(dimethyl siloxane) (PDMS) film stamping method[19] that eliminates assumptions about photoacid diffusion across different media.[11] This improvement enabled deprotection reaction-diffusion kinetics during the PEB as measured by FTIR combined with mean-field modeling. The photoacid diffusion length was smaller in a calix[4]resorcinarene-based resist[19] than in a chemically similar polymer resist that favors a smaller CD. Furthermore, the developed mean-field reaction kinetics model considered photoacid diffusion, the deprotection reaction rate constant, and a phenomenological photoacid trapping rate constant that provide metrics that may be included in theory and simulation models.[20−24] The methods were extended to ring-like, disk-like, and branched molecular resist architectures with reaction constants correlated to the protection group molar density.[25] These FTIR reaction kinetics methods, however, do not measure the nanometer-scale reaction front but rather the average reaction kinetics with the bilayer approach.

In this article, the nanometer-scale in situ latent image profiles are measured using neutron reflectivity for a model molecular resist system of deuterium-labeled *tert*-butoxycarbonyloxy (d-tBoc)-protected methyl-calix[4]resorcinarenes (d-tBoc-CM4R). These neutron reflectivity measurements demonstrate that even though d-tBoc-CM4R are smaller imaging materials the reaction-front latent image width exceeds the $R_g$. The spatial extent of the reaction front increases but has a reduced effective diffusion at long PEB reaction times. This behavior can be reconciled by the photoacid trapping process that was developed independently by complementary FTIR reaction kinetics. In addition to the latent image, the developed image was also examined as both an aqueous-based positive tone and a solvent-based negative tone. Materials with dual tones, such as the PBOCSt system,[2] are finding increased interest in light-field masks and spacer-assisted double patterning.[26,27] The d-tBoc-CM4R latent images were measured after positive- and negative-tone development, with roughness remaining in both cases even with the ideal step exposure. Insight into the development mechanism of the line

edge is described and compared to polymer resists. Finally, the limitations in the mean-field reaction-diffusion model are also described in the context of reaction-limited transport.

## 2. MATERIALS AND METHODS

**2.1. Molecular Resist Materials.** All reagents were used as received from the suppliers without further purification unless otherwise noted. 1,4-Diazabicyclo[2.2.2]octane (DABCO) was recrystallized from petroleum ether. Acetone used in reactions was dried over 3 Å activated molecular sieves. The all-cis (ccc) stereoisomer of tetra-*C*-methylcalix[4]resorcinarene (**CM4R**) was prepared as described. ^{1}H and ^{13}C NMR were in agreement with the literature[28,29] and confirmed the identity as the ccc isomer. $(CD_3)_3COH$ was prepared from $CD_3I$ and acetone-$d_6$ as described.[30]

*2.1.1. Analytical.* Proton and carbon nuclear magnetic resonance spectra were obtained at room temperature on a Varian VNMRS 500 NMR spectrometer (operating at 499.717 MHz for protons) at the Center for Nanophase Materials Sciences at Oak Ridge National Laboratory. Spectra recorded in $CDCl_3$ were referenced to internal tetramethylsilane (0 ppm) for proton spectra and to 77.23 ppm for carbon spectra; carbon spectra recorded in acetone-$d_6$ were referenced to the center of the septet at 29.92 ppm. Thermogravimetric analyses were performed on a TA Instruments Q5000IR thermogravimetric analyzer.

*2.1.2. Di-tert-butyl Tricarbonate-$d_{18}$.* The deuterated analog was prepared from $(CD_3)_3COK$ (prepared from $(CD_3)_3COH$ and KH in THF) following the procedure described for the nondeuterated di-*tert*-butyl tricarbonate,[31] with the following modifications. For safety reasons, a 20% solution of phosgene in toluene was used instead of phosgene gas bubbled into benzene (**Caution!** *Phosgene is very toxic, and all manipulations with phosgene must be conducted in a well-ventilated fume hood!*) Anhydrous carbon dioxide from a lecture bottle was further dried by passage first through a Drierite gas purifier (containing Drierite and 5 Å molecular sieves) and then passage over concentrated sulfuric acid, followed by passage over powdered phosphorus pentoxide before exiting into a wide-bore bubbling tube inserted into the reaction mixture. Nitrogen used in the reaction to flush out the phosgene was dried by passage through a Drierite gas purifier. Typical yields after recrystallization from pentane at −20 °C were 43−59%. (The literature value yield is 59−62% for di-*tert*-butyl tricarbonate-$h_{18}$.[31]) The material was stored under nitrogen in a −20 °C freezer until used in the subsequent step. ^{13}C NMR ($CDCl_3$) $\delta$: 26.5 (septet, $J_{CD}$ = 19.5 Hz, $-CD_3$), 87.1 ($-C(CD_3)_3$), 143.5 (center carbonyl carbon), 144.9 ($-OC(O)-O-C(CD_3)_3$).

*2.1.3. Di-tert-butyl Dicarbonate-$d_{18}$.* The deuterated analog was prepared from recrystallized di-*tert*-butyl tricarbonate-$d_{18}$ above following the literature procedure.[31] Final purification was by vacuum distillation (47−48 °C at 0.10 Torr) to yield a colorless liquid that solidifies on standing. Typical yields were 86−89% (literature values of 80−91% for di-*tert*-butyl dicarbonate-$h_{18}$[31]). The compound was stored under nitrogen in a 3 °C refrigerator until ready to use. ^{13}C NMR (acetone-$d_6$) $\delta$: 26.5 (septet, $J_{CD}$ = 19.3 Hz, $-CD_3$), 85.4 ($-C(CD_3)_3$), 147.7 ($-OC(O)-O-C(CD_3)_3$).

*2.1.4. Octa-O-tert-butyl-$d_{72}$ Carbonated C-Methyl-calix[4]-resorcinarene.* The ccc isomer of tetra-*C*-methylcalix[4]resorcinarene (2.56 g, 4.70 mmol) and a catalytic amount of 4-dimethylaminopyridine (DMAP, 0.057 g, 0.47 mmol) were suspended in 35 mL of acetone in a 100 mL flask. With stirring, a solution of di-*tert*-butyl dicarbonate-$d_{18}$ (11.2 g, 47.0 mmol) in 5 mL of acetone was slowly added dropwise. Over a 20 min period of stirring at room temperature, the solution color changed from burgundy red to very pale yellow, with considerable gas evolution that ceased at the end of the 20 min. The solution was stirred for an additional 20 min, after which the volatiles were removed by rotary evaporation at 40 °C. The residue was recrystallized from 230 mL of 9:1 v/v 2-propanol/acetone to afford a first crop of 5.05 g (76%, assuming a MW of 1417.97 for full functionalization) of white microcrystalline material that, after being vacuum dried at room temperature, was analytically pure for the compound, with no trace of residual DMAP by NMR. ^{1}H NMR

(CDCl$_3$) $\delta$: 1.45 (d, $J$ = 7.1 Hz, 12 H, $-CH_3$), 4.45 (q, $J$ = 7.1 Hz, 4 H, $-CH$), 6.9 (very br s, aromatic hydrogens, 8H). $^{13}$C NMR (CDCl$_3$) $\delta$: 20.7 ($-CH_3$), 26.9 (septet, $J_{CD}$ = 19.0 Hz, $-CD_3$), 31.6 ($-CH$), 82.3 (*tert-C*), 116.5, 125.9, 134.2, 147.1 (aromatic carbons, all broad, some very broad), 151.7 (C=O). Cooling the mother liquor to $-18$ °C afforded an additional 0.88 g of nearly pure material, which after recrystallization afforded 0.80 g (12%) of analytically pure material for a combined yield of 88%.

*2.1.5. Average 80 mol % O-tert-Butyl-d Carbonated C-Methylcalix[4]resorcinarene (80d-tBoc-CM4R).* The nominally 80% protected CM4R was prepared following the manner described above, with less di-*tert*-butyl dicarbonate-$d_{18}$ being used. To the ccc isomer of *tetra-C*-methylcalix[4]resorcinarene (4.36 g, 8.00 mmol) and a catalytic amount of 4-dimethylaminopyridine (DMAP, 0.098 g, 0.8 mmol) suspended in 50 mL of acetone in a 100 mL flask was slowly added dropwise under nitrogen with stirring a solution of di-*tert*-butyl dicarbonate-$d_{18}$ (12.41 g, 52.5 mmol, for nominally 82% functionalization) in 5 mL of acetone. Over a ca. 20 min period, the solution bubbled as above, but the initial burgandy color remained. The solution was stirred at room temperature overnight, during which time the burgandy color remained, and the volatiles were removed by rotary evaporation at 40 °C. The purple-red residue was purified by chromatography (SiO$_2$, 1:1 hexanes/ethyl acetate) to afford after solvent removal 8.75 g (approximately 87% yield based on the protection level) of a pale-yellow solid. The proton and carbon NMR spectra are quite complex because of the many different substitution possibilities spanning the range of $^5/_8$ to full functionalization but show no trace of residual DMAP. $^1$H NMR (CDCl$_3$) $\delta$: 1.44–1.48 (overlapping doublets, 12 H for all, $-CH_3$), 4.23, 4.45, 4.51 (each q, $J$ = 7.1 Hz, 4 H in total in an approximately 1.6:2.8:1.6 ratio, respectively, $-CH$). There are many single peaks of varying intensity for the aromatic protons plus a broad peak at 6.9 ppm with the following integrations: 5.41 (0.86H), 5.52 (0.13H), 6.08 (1.00H), 6.19 (0.65H), 6.42 (0.14H), 6.59 (0.10H), 6.72 (0.14H), 6.75 (0.58H), 6.86 (0.1H), 6.9 (very broad, about 1.2H), 6.96 (0.1H), 7.07 (1.03H), 7.11 (0.64H), 7.17 (0.1H), 7.22 (0.14H), 7.38 (0.68H). $^{13}$C NMR (CDCl$_3$) $\delta$: 20.1 20.4, 20.7 ($-CH_3$), 26.9 (br septet, $J_{CD}$ = 19.0 Hz, $-CD_3$), 31.6, 32.0, 32.3 ($-CH$), 82.6, 83.0, 83.4, 83.7 (*tert-C*), 108.4, 115.7, 116.5 (br), 117.1, 122.3, 124.4, 125.9 (br), 126.2, 126.4, 132.7, 134.2 (very br), 136.1, 137.4, 146.6, 146.8, 147.1 (very br), 147.7 (aromatic carbons, most are sharp, the others from the small amount of fully functionalized material are broad as noted), 151.4, 151.7 (br), 152.1, 152.7, 153.8 (C=O). Thermogravimetric analysis showed an average mass loss corresponding to a deuterated tBoc protection level of 80%.

**2.2. PDMS Film-Transfer Methods.** The procedure for preparing these bilayer films involves three major steps: spin coating of the bottom layer, stamp fabrication, and stamp film transfer. For positive-tone sample preparation, the bottom layer film that does not contain PAG should be prepared beforehand on clean silicon wafers and postapply baked to remove residual solvent. By removing the residual solvent, the interdiffusion of the two layers during the stamping process is minimized. The PDMS stamp with a thickness of less than 5 mm is prepared from a commercially available PDMS prepolymer (Dow Corning Sylgard 184 base and curing agent) with cross-linker in a 10:1 or 12:1 mass ratio. The liquid mixture is stirred for 15 min until it becomes opaque and is then poured onto a separate clean silicon wafer that rests inside a larger dish. Typically, a 5 mm stamp works well and has sufficient mechanical properties. This entire dish is placed into a vacuum chamber to remove air bubbles, after which the PDMS is cured in a preheated oven at 70 °C for 1 h. The PDMS stamp is then cooled to room temperature. A circular piece is cut using a razor blade and peeled off of the silicon wafer. This smooth surface that was in contact with the wafer is the top of the stamp. To improve the wetting properties for spin coating the resist solutions onto the PDMS stamp, the PDMS surface is treated with oxygen plasma for 5 s at an oxygen flow rate of 2 SCFH. The stamp can then be placed onto a spin coater to prepare the top-layer film (nominally 80 to 300 nm thick) without a subsequent bake. Freshly prepared stamps perform better.[32] Finally, the film is transferred from the PDMS substrate to the bottom layer by gently resting the film side on the bottom-layer film making contact between the two polymer films. After ~10 min, PDMS should be in full contact with the bottom-layer film and should be transferred to a hot plate preheated to 90 °C. The PDMS stamp is gently compressed for about 20 s, and then the sample is removed and allowed to cool. The PDMS stamp is then slowly peeled off. The transferred film forming the bilayer stack was PAB for 60 s at the same PAB temperature used for the bottom layer to remove residual solvent in the top layer.

**2.3. Exposure and Development.** An Oriel UV exposure system was used for the reaction kinetics studies at a dose of ~150 mJ/cm$^2$ with 248 nm broadband radiation. At these exposure doses, all of the photoacid generators were activated. PEB was performed with a CEE hot plate setup with vacuum contact. Positive-tone samples were developed under ambient conditions in 0.26 mol/L tetramethylammonium hydroxide for 60 s, rinsed with deionized water for 60 s, and spin dried. Negative-tone samples were developed in hexane for 60 s and spin dried.

## 3. RESULTS

**3.1. Neutron Reflectivity and Ideal Lithographic Line Edge.** The approach to mimicking a step-exposure line edge involves forming two thin films into a bilayer stack without intermixing.[19] A PAG-containing d-tBoc-CM4R film was prepared by spin coating on a PDMS substrate and then transferring by film stamping on a PAG-free d-tBoc-CM4R film as shown in Scheme 1 with details provided in Materials and Methods. This provides a step concentration in PAG between films within one diffusion medium, improving upon previous bilayer approaches.[11] The stamping method forms a sharp interface between two identical layers with an interfacial width of less than 1 to 2 nm as measured by neutron reflectivity with a bilayer of deuterated and protonated poly(methyl methacrylate). Therefore, the PAG appears as a near-step profile within length scales of the interfacial width. The PAG is present in the top layer for the positive tone because the top layer will react and become soluble in an aqueous base developer whereas with negative tone the PAG is placed in the bottom because the unreacted d-tBoc-CM4R would be solvent-developed (Scheme 1).

Specular neutron reflectivity was performed on the NG7 horizontal cold neutron reflectometer at the NIST Center for Neutron Research. The reflectivity was normalized by the incident beam intensity and measured as a function of the wave vector ($Q$) normal to the film, $Q = (4\pi \sin \theta)/\lambda$, where $\lambda$ is the incident neutron wavelength of 4.75 Å and $\theta$ is the specular angle of reflection. The specular reflected intensity provides a nanometer-resolution depth profile of the film due to neutron scattering length density variations (contrast). The scattering length density (SLD) is quantified by the total scattering length ($b = \sum_i b_i$ over all atomic elements per molecule) within the molecular volume ($v$) and is often reported as $b/v$ or SLD. Although the atomic scattering length ($b_i$) varies from element to element, a large scattering length difference occurs between hydrogen ($b_H = -0.374 \times 10^{-12}$ cm) and deuterium ($b_D = 0.667 \times 10^{-12}$ cm) isotopes. Therefore, the contrast in a neutron reflectivity experiment may be enhanced by deuterium substitution to measure composition profiles with nanometer resolution. The reflectivity data were fit using the Parratt algorithm with the NIST Reflpak software.[33] In general, this approach calculates the reflectivity resulting from successive slab layers of constant scattering length density with interfaces smeared by a Gaussian function. When the slab fit parameters are varied (scattering length density, absorption, thickness, and

**Scheme 1. (a) Positive-Tone Schematic of the Sample Preparation of the Model Lithographic Line Edge on Silicon Wafers[a] and (b) Negative-Tone Sample Preparation[b]**



**(a) Positive-tone**



**(b) Negative-tone**
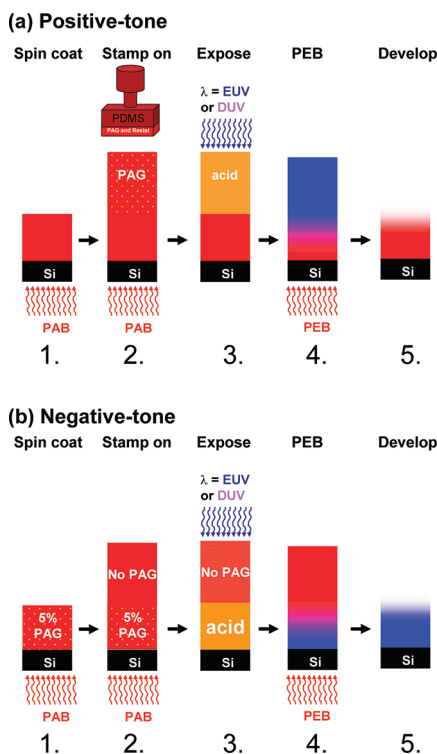


[a]Step 2 involves film transfer of the PAG-containing film from a PDMS stamp on the PAG-free layer prepared in step 1. Subsequent exposure (with 13.5 nm EUV or 248 nm broadband DUV light) involves PEB and TMAH development.

[b]Step 2 involves film transfer of the PAG-free film from a PDMS stamp on the PAG-containing layer prepared in step 1. Subsequent exposure and PEB allow high-resolution characterization with neutron reflectivity of the latent and developed image followed by negative-tone development (hexane).

roughness), a multilayered model can be established to determine the best $\chi^2$ fit to the reflectivity data. An estimation of the total error in the extracted fit parameters (SLD and film profiles) is difficult because the precision of the fit parameters, determined by the inverse of the curvature matrix, is in general less than the significant figures reported.[34] Uncertainties in the reflectivity data are calculated as the estimated standard deviation from the mean. In the case where the limits are smaller than the plotted symbols, the limits are removed for clarity.

Deuterium-substituted *tert*-butoxycarbonyl (t-Boc) protecting groups were synthesized. Each calix[4]resorcinarene has a maximum of eight hydroxyl moieties for protection. This is in contrast to polymer resists that are polydisperse in molecular mass and protection substitution. Calculations of the SLD versus the number of t-Boc's per CM4R are shown as the solid symbols in Figure 1 for perdeuterated t-Boc and hydrogenous t-Boc-protected CM4R. The calculations used the molecular volume determined experimentally from the mass densities of 100, 0, and average 80% t-Boc pure-component film controls. A calibration curve was prepared to interpolate the mass-density dependence of t-Boc substitution. The hashed symbols are the experimentally determined SLD for partially reacted thin films with an average extent of deprotection determined by FTIR.
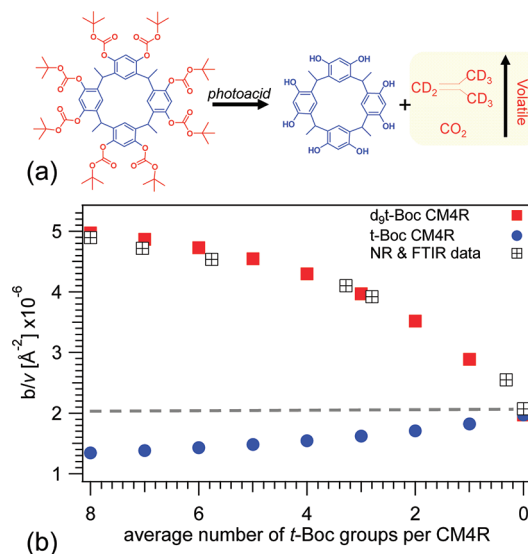


**(a)**



**(b)**

**Figure 1.** (a) Photoacid-catalyzed deprotection of d-tBoc-CM4R shown with a majority of volatile products (carbon dioxide and deuteroisobutene). The extent of reaction is dependent upon the reaction kinetic conditions. (b) Calculated and measured neutron scattering length densities as a function of the number of t-Boc groups per CM4R. Specially synthesized deuterium-substituted t-Boc and protonated t-Boc reagents separately protected the same parent CM4R. The uncertainties are smaller than the symbols and do not exceed 5%.

The experiment and model agreement allow a mapping of SLD to the fraction of the d-tBoc-CM4R protection level. In this study, the reaction front studies consider only the 100% d-tBoc-CM4R.

**3.2. Positive-Tone Latent Image.** Figure 2 shows the neutron reflectivity data for a bilayer prepared with d-tBoc-
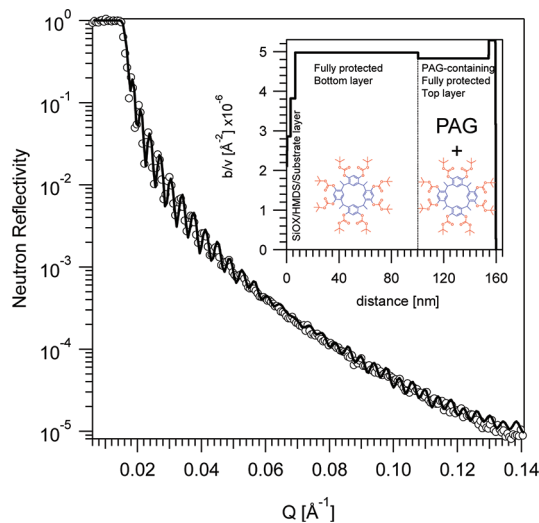


**Figure 2.** Reflectivity from a film composed of *d*-CM4R with 5% PAG on top of *d*-CM4R without PAG on the silicon wafer. Inset: Scattering length density profile from the silicon substrate.

CM4R with triphenylsulfonium (TPS) perfluorobutanesulfonate (PFBS) (TPS-PFBS) PAG on top of d-tBoc-CM4R before ultraviolet (UV) exposure and postexposure bake. The reflectivity was model fit using standard procedures with slabs for the silicon (with average SLD = $(2.17 \pm 0.08) \times 10^{-6}$ Å$^{-2}$),

**Table 1. Summary of Latent Image Characteristics and Developed Roughness Determined by Neutron Reflectivity for Positive- and Negative-Tone Bilayer Samples for Several PEB Conditions**

| | bilayer structure[a] | PEB time (s), 80 °C | latent image | | | developed image |
| | | | error function width (nm) | LILS (nm$^{-1}$)[b] | $L_d$(nm)[ce] | roughness (nm)[d] |
|---|---|---|---|---|---|---|
| positive tone DUV exposure | PAG+100d / 100d | 4 | 12.9 | 0.051 ± 0.003 | 0.4 | incomplete |
| | | 8 | 11.1 | 0.11 ± 0.006 | 7.0 | incomplete |
| | | 15 | 10.9 | 0.20 ± 0.01 | 3.7 | incomplete |
| | | 60 | 9.0 | 0.34 ± 0.04 | 8.2 | 2.2 |
| | | 30 | 11 | 0.23 ± 0.03 | 9.6 | 3.4 |
| | | 60 | 11.3 | 0.29 ± 0.05 | 9.8 | 2.5 |
| | | 90 | 6.7 | 0.43 ± 0.05 | 6.9 | 2.5 |
| | | 120 | 4.6 | 0.68 ± 0.09 | 8.1 | 2.7 |
| | | 180 | 6.1 | 0.60 ± 0.07 | 9.2 | 2.4 |
| negative tone DUV exposure | 100d / PAG+100d | 30 | 15.2 | 0.13 ± 0.01 | 1 | 4.2 |
| | | 60 | 9.9 | 0.21 ± 0.02 | 1.1 | 3.3 |
| | | 120 | 8.3 | 0.22 ± 0.03 | 6.7 | 3.3 |
| | | 180 | 6.4 | 0.29 ± 0.03 | 12.9 | 3.0 |

[a]The film[1]/film[2] structure implies film[1] stamped on film[2] on a silicon wafer. [b]LILS for positive tone taken as $1/\phi(d\phi/dz)|_{\phi=0.25}$ where $\phi$ = 0.25 at the solubility switch, with the uncertainty estimated from 1 standard deviation of the slope of the deprotection profile. For negative tone, $\phi$ = 0.5. [c]Uncertainty estimated as ±1 nm on the basis of the uncertainty in the bilayer film thickness. [d]Determined by neutron reflectivity as the error-function width parameter at the air/film interface. [e]Positive tone: estimated by the change in distance from the midpoint of the reaction front to the initial bilayer interface. Negative tone: estimated by the change in distance from the midpoint of the reaction front to the initial top-layer thickness.

silicon oxide (with average SLD = $(3.00 ± 0.18) × 10^{-6}$ Å$^{-2}$ and thickness = 1.8 ± 0.4 nm), substrate layer, and bilayer film with a bottom-layer thickness of ~97.5 nm and a top layer thickness of ~50 nm. Because the top layer contains protonated PAG, the SLD was slightly lowered to fit the data. A slab of lower SLD at the substrate interface and a slab of higher SLD at the air/film interface were necessary for the fits. These two thin layers (compared to the bulk of the film) are responsible for the pinch and loss of the reflectivity fringes (0.05 Å$^{-1}$< Q < 0.08 Å$^{-1}$) rather than surface roughness at the resolution used for the experiment.

After exposure to UV light, the PAG undergoes photolysis,[2] producing perfluorobutanesulfonic acid (PFBS) in the top layer. Therefore, a photoacid step concentration change occurs at the bilayer film interface. This step change provides an initial condition that mimics the step exposure in a lithographic line edge.[4,6,11] The matrix of samples with different PEB reaction times and film stack preparations is shown in Table 1. After the PEB, each film was analyzed with infrared spectroscopy and infrared reflectance variable-angle spectroscopic ellipsometry[35] to determine the average changes in protection and thickness, respectively. Figure 3 shows neutron reflectivity results for four different PEB times at 80 °C. As the deprotection reaction proceeds, the loss of volatile deuterium protection products lowers the average SLD of the film, consistent with the expectations of Figure 1. However, a surface and bulk extent of reaction was observed. The molecular resist exhibits a reduced extent of reaction at the surface as observed by the persistent high SLD with reaction time, whereas the bulk film shows a reduced SLD. The reduced surface reaction was also observed in PEB processed thin films of TPS-PFBS d-tBoc-CM4R blends, therefore ruling out an artifact of the film-stamping process.[36] The diffuse interface between the bulk reaction of the top layer and the PAG-free bottom layer is the reaction front (latent image). At the longest PEB times (120 and 180 s) prepared with different initial bottom-layer thicknesses (~59 nm), the reaction front remains diffuse with error-function widths of 4.5 and 5.5 nm, respectively, as shown in the SLD
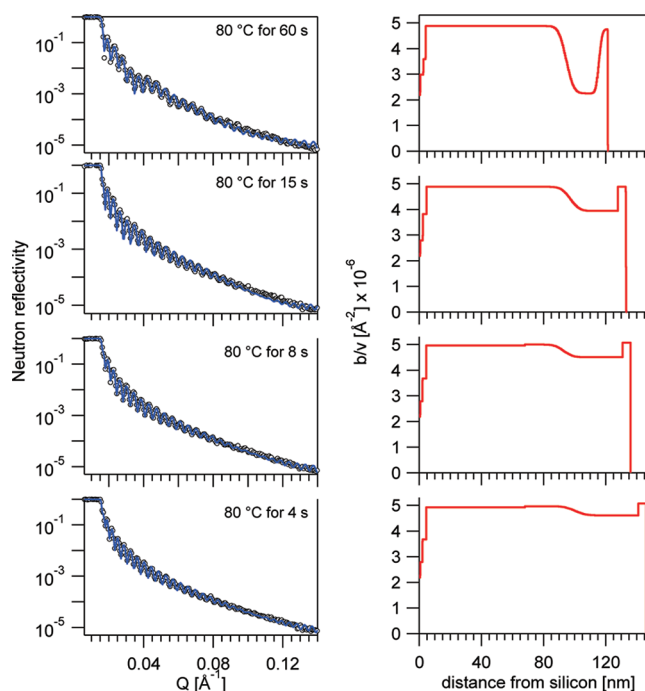


**Figure 3.** (Left) Fresnel-normalized neutron reflectivity with Parratt model fits (solid lines). (Right) Associated scattering length density profiles of the latent images for an ultraviolet-light-exposed, PEB-baked (80 °C) bilayer film for shorter PEB times. The surface-inhibited reaction occurs at the free surface of the film, whereas the reaction front and bulk extent of reaction are identified.

profiles in the solid lines of Figure 4. In these cases, the top layer was completely deprotected and therefore kinetically limited as the surface layer extent of reaction lagged behind that of the bulk (reflectivity in Supporting Information).

**3.3. Negative-Tone Latent Image.** Negative-tone samples were prepared with the PAG in the bottom layer and the PAG-free layer on top. After UV exposure through the entire film stack, the PAG in the bottom layer was fully exposed. Neutron
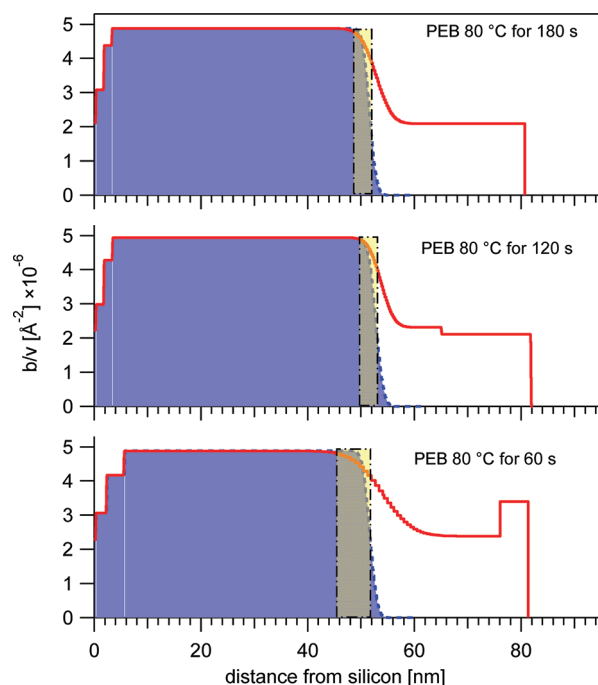
**Figure 4.** Scattering length density profiles of the latent and positive-tone TMAH developed images for ultraviolet-light-exposed, PEB-baked (80 °C) bilayer films. The highlighted region defines the fraction of resist that undergoes a development-induced restructuring leading to the final roughness.



**Figure 5.** Scattering length density profiles of the latent and negative-tone hexane developed images for ultraviolet-light-exposed, PEB-baked (80 °C) bilayer films. The highlighted region defines the fraction of resist that undergoes a development-induced restructuring leading to the final roughness. The hexane developer dissolves higher deuterium t-Boc-protected CM4R, leaving more weakly deuterium-protected CM4R material as observed in the developed image profile that is lower than the latent image profile.

reflectivity measurements were performed for PEB times ranging from 30 to 180 s. In this case, the volatile deprotection products (deuteroisobutene and $CO_2$) must be transported through the bilayer. The influence of airborne amine quenching of the photoacid and amine contamination was minimized with the PAG in the bottom layer because the film absorption rate of amines exposed to photoacid must pass through a relatively thick (hydrophobic) top layer.[37] Initially, the role of amine was speculated to cause the surface-reduced layer, but in fact, longer delays did not decrease the extent of reaction, as observed in separate infrared spectroscopy experiments.

The SLD profiles for three PEB times are shown as the solid lines in Figure 5. In this case, the bottom layer is highly deprotected after 60 s with bulk SLD ≈ 2.19 × 10$^{-6}$ Å$^{-2}$. In these cases, there is no low SLD substrate layer of only silicon (with average SLD = (2.09 ± 0.03) × 10$^{-6}$ Å$^{-2}$) and silicon oxide (average SLD ≈ (3.13 ± 0.03) × 10$^{-6}$ Å$^{-2}$ and thickness = 0.8 ± 0.2 nm). Further from the silicon substrate, the SLD increases through the reaction front and plateaus at the 100% d-tBoc-CM4R value, followed by the sharp film/air interface, even after long reaction times. The error function interfacial width of the reaction front systematically changes from 14.9 to 9.7 to 9.1 to 7.1 nm for 30, 60, 120, and 180 s PEB times, respectively. Independent infrared spectroscopy quantifies the increase in the extent of deprotection with increased PEB times.

**3.4. Positive-Tone and Negative-Tone Developed Images.** The films were developed in positive tone by 0.26 mol/L tetramethylammonium hydroxide (TMAH) solution. Samples with PEB times of 0, 4, 8, and 15 s did not dissolve because of the highly protected surface layer. The surface layer did not inhibit dissolution for the longer-reacted films (typically greater than 30−60 s). The developed and dried neutron reflectivity data are shown in the Supporting Information. The
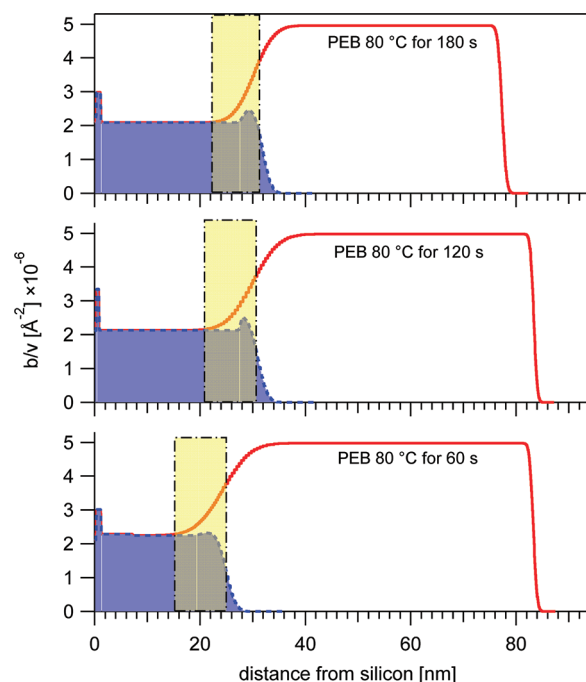
SLD profiles for developed (dotted line) bilayers are plotted along with the corresponding latent image (solid line) in Figure 4. The highly deprotected top layer was dissolved in TMAH along with a portion of the diffuse reaction front, leaving a compositionally sharp developed film. After TMAH development, the substrate layers did not require any SLD adjustment during the fitting process; therefore, the development and transport of the TMAH and water were confined to the soluble top-reacted layer and reaction-front interface. The developed surface roughness values were 3.4, 2.5, 2.7, and 2.4 nm for 30, 60, 120, and 180 s PEB samples, respectively, as determined by neutron reflectivity. One 60 s PEB sample was measured by X-ray reflectivity and had a surface roughness of 2.5 nm, suggesting little difference in the compositional and mass density roughness. Atomic force microscopy observed a root-mean square surface roughness of 1.5 nm (Supporting Information).

Negative-tone development with hexane dissolves 100% d-tBoc-CM4R but not unprotected CM4R. After development, the reflectivity data are more complex than a single layer (Supporting Information). The developed film SLD profiles in Figure 5 show that the top d-tBoc-CM4R dissolves along with a fraction of the reaction front, leaving highly deprotected CM4R (dotted line). The total film thickness of the developed film is observed. However, when comparing the developed to latent image (solid line) SLD profiles, we find that a divergence in SLD occurs well before the total film thickness is reached. Contrary to the positive-tone development, the reaction-front interface does not etch back (dissolve) to an average extent of deprotection with an unchanged interfacial zone. As shown in Figure 5 for PEB of 60 s, the remaining developed film has a

low extent of deprotection with SLD ≈ 2.19 × 10$^{-6}$ Å$^{-2}$. However, at the same depth of 22 nm the latent-image SLD profile has a higher SLD. Therefore, molecular resists of high deuterium t-Boc protection selectively dissolve in hexane, leaving behind insoluble CM4R. Under an ideal soluble-to-insoluble dissolution switch, the developed SLD profile should continuously track the latent image until the point of development or average composition for solubility; this is not observed in negative-tone development. This is evidence that an etch-only dissolution mechanism is not accurate on the nanoscale for negative tone.

Furthermore, for PEB of 120 and 180 s, an increase in the SLD is observed at the surface between 28 and 30 nm depth profile thicknesses, respectively. This thin layer of higher SLD material is insoluble and is a result of the development process. The average deuterium composition was between 0 and 1 t-Boc substitution per CM4R. Therefore, organic solvent negative-tone development allows CM4R to restructure by selectively removing higher d-tBoc-protected CM4R and leaving behind the lowest protected CM4R. The developed surface roughnesses were 4.2, 3.3, 3.3, and 3.0 nm for the 30, 60, 120, and 180 s PEB samples, respectively, as determined by neutron reflectivity; these were systematically higher than positive-tone development at equivalent PEB times but involved an entirely different dissolution mechanism.

## 4. DISCUSSION

### 4.1. Substrate and Surface Structure.
The interface between the bilayer and silicon substrate is composed of silicon oxide primed with hexamethyldisilazane (HMDS) and a low-SLD substrate layer. This discrete substrate layer has an SLD greater than that of native silicon oxide and HMDS but lower than that of 100% d-tBoc-CM4R. Because analytical characterization showed 100% d-tBoc substitution, the presence of a phase-segregated lower-protected impurity was ruled out. Residual protonated solvent that adsorbed to the substrate and mixed with the CM4R is a possibility, but one expects a diffuse interface, not a discrete layer of low interfacial width. Because all films undergo thermal treatment, thermal deprotection is possible. However, it also should cause a diffuse interface. Rather, we speculate that this is a reduced-density layer of d-tBoc-CM4R at the confined substrate. For samples exhibiting a substrate layer (positive tone, PEB kinetics), the average SLD was (3.98 ± 0.2) × 10$^{-6}$ Å$^{-2}$ with a thickness of (2.2 ± 0.8) nm or 1 to 2 CM4R molecular diameters. These observations may be reminiscent of deviations in dynamics within a few $R_g$ for polymers confined to thin films. However, in this case the observations imply a reduced mass density of 18% from the fully protected value of 1.16 g/cm$^3$. Although purified d-tBoc-CM4R can crystallize, the substrate layer has a lower SLD than does the crystalline form. Furthermore, the layer is eliminated by reaction during the negative-tone experiments as deprotection occurs close to the substrate (Figure 5).

The higher SLD at the surface appears at short PEB times at 80 °C with an average SLD of (4.8 ± 0.2) × 10$^{-6}$ Å$^{-2}$ and a thickness of 5.2 ± 0.2 nm. This SLD is less than 100% d-tBoc-CM4R but is consistent with a blend of CM4R and hydrogen-containing PAG. However, the reactivity at the surface was reduced compared to that of the bulk. A similar reduced surface reaction was observed in polymer photoresists by near-edge X-ray fine structure spectroscopy.[38,39] The influence of a postexposure delay and atmospheric contamination was

consistent with the observations; however, the presence of surface ordering also contributes,[36] as observed with PAG- and 100% d-tBoc-CM4R-reacted thin films. Thin films of epoxy observe a nonuniform distribution of cross-linker[40] and therefore extent of reaction. The partitioning of reactive additives in thin films such as PAGs[39,41] is beyond the scope of this article, but as experimentally observed, this surface layer becomes less in magnitude at longer reaction times and therefore is a transient but important observation.

### 4.2. Spatial Extent of Reaction Front: Effective Diffusion.
The spatial progression and shape of the reaction front is related to the ultimate resolution of the resist. Pawloski et al.[6] showed that an increase in the latent image log slope (LILS), a measure of the shape of the reaction front, leads to reduced roughness that plateaus at large image slopes. Furthermore, the photoacid diffusion length ($L_d$) must be less than the expected feature size. Routes to reduce $L_d$ include varying the size of the photoacid[13] as well as covalently bonding the PAG to the resist to restrict diffusion.[42-45] In the current demand for high-throughput, resists with higher sensitivity to lower exposure doses ($E_o$) is also a design criterion. The following relationship was proposed to generalize resist resolution metrics and is related to the line-edge roughness (LER)[46-49]

$$LER \approx \frac{1}{\sqrt{\alpha E_o}} \frac{1}{\sqrt{\varepsilon}} \frac{1}{LILS \cdot L_d^{\Delta}} \qquad (1)$$

where $\alpha$ is the fraction of light absorbed by the resist film, $\varepsilon$ is the PAG quantum efficiency, and $\Delta$ is predicted to be 1, $^3/_2$, or 3.[16] The photoacid diffusion length is related to the effective diffusion constant ($D_{eff}$) by $L_d = (4D_{eff} t_{PEB})^{1/2}$. $L_d$ and LILS compose the spatial extent and shape of the deprotection profiles, respectively, as measured by neutron reflectivity (Table 1). After the SLD profiles were converted into real-space deprotection profiles, the $D_{eff}$ was estimated from the known $t_{PEB}$ and $L_d$ determined by the distance between the initial bilayer interface and the midpoint of the error function profile interface. Figure 6 shows the PEB reaction time dependence of $D_{eff}$. The effective diffusion constant appears to go through a maximum and then plateaus at the longest reaction times. When we averaged over the three longest PEB times, we obtained $D_{eff}$ = 0.13 ± 0.06 nm$^2$/s, which was lower than the photoacid diffusion constant of 0.525 nm$^2$/s determined by the infrared spectroscopy reaction kinetics study of these deuterated materials. For a simple Fickian diffusive process (no reaction), $D_{eff}$ should not depend upon the reaction time, which is not representative of the data. It is plausible that the origin of the variability in $D_{eff}$ could be experimental. For instance, the initial condition of the PAG may not be a step function but may be broadened by the sample preparation heating process, even though the annealing conditions are below the nominal $T_g$ of d-tBoc-CM4R. In such a case, the presence of PAG beyond the initial bilayer interface could lead to a seemingly rapid diffusion process. The shortest PEB time of 4 s had an $L_D$ of 0.4 nm, leading to a low effective diffusion coefficient. However, because the reaction-diffusion equations are nonlinear, trends were examined within the kinetic constant parameter space guided by these experimental trends.

Model calculations were performed using the coupled differential equations that describe the spatiotemporal change in the t-Boc deprotection level, $\phi(x, t)$, and acid concentration, $H(x, t)$ as described in Kang et al.[19] $\phi = 0$ corresponds to fully
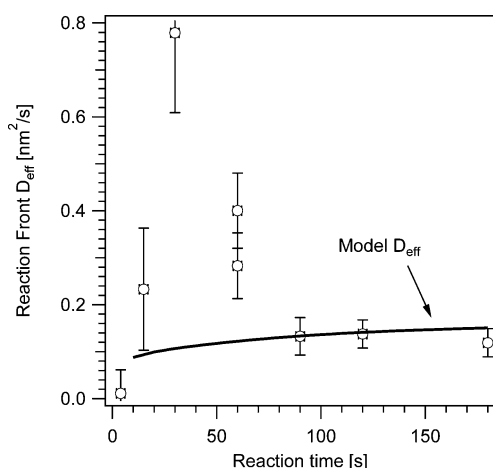
**Figure 6.** Symbols show the effective reaction-front diffusion coefficient estimated by the spatial extent of reaction from the initial bilayer interface. The error bars in $D_{eff}$ are estimated by propagating an uncertainty in the PEB time ($\pm 2$ s) and location ($\pm 1$ nm) of the bilayer interface. The solid line represents the $D_{eff}$ calculated from the reaction front by solving the mean-field reaction-diffusion equations with parameters ($k_P = 0.632$ nm$^3$/s, $k_T = 0.0257$ s$^{-1}$, $D = 0.525$ nm$^2$/s) determined by FTIR methods.

t-Boc-protected (left side of reaction in Figure 1a), and $\phi = 1$ is fully deprotected.

$$\frac{d\phi(x, t)}{dt} = k_P(1 - \phi(x, t))\, H(x, t) \qquad (2)$$

$$\frac{\partial H(x, t)}{\partial t} = D\frac{d^2 H(x, t)}{dx^2} - k_T H(x, t)\, \phi(x, t) \qquad (3)$$

Equation 2 is the first-order reaction kinetics with deprotection reaction rate constant $k_P$. Equation 3 describes the diffusive flux of the photoacid with constant photoacid

diffusivity ($D$). The second term in eq 3 is the photoacid trapping rate such that the effective acid concentration decreases with time with rate constant $k_T$ because the trapping probability is the product of $\phi(x, t)$ and $H(x, t)$. Therefore, there is an increasing probability that the acid concentration is reduced as the reaction proceeds. The initial conditions are a step change in $H(x, t)$ across the bilayer interface with an initial concentration $H_o(x, 0)$. The Neumann boundary conditions are $d\phi/dt = 0$ and $dH/dt = 0$. The reaction constants for the deuterated materials determined in this work using methods described previously[19] are $k_P = 0.632$ nm$^3$/s, $k_T = 0.0257$ s$^{-1}$, and $D = 0.525$ nm$^2$/s. The calculated deprotection profiles are shown in Figure 7 with and without the trapping constant ($k_T$) for PEB times of 2 to 200 s and different ratios of $k_P/D$ as detailed in the caption. In the absence of the trapping constant ($k_T = 0$) in Figure 7a−c, the deprotection profile propagates unbounded because the initial acid concentration spreads diffusively. However, for the same $k_P$ and $D$ but $k_T = 0.0257$ s$^{-1}$ the profiles, upon comparison, have a reduced spatial extent and tend to slow down with time and become pinned.

The ratio of the reaction constant to the photoacid diffusion constant ($k_p/D\Lambda$) is the Dahmköhler dimensionless number[50] within a characteristic length $\Lambda$. Therefore, the ratio $k_p/D$ describes the velocity of the reaction-diffusion process. $k_p/D\Lambda \gg 1$ implies that the diffusion velocity is smaller than the reaction velocity; therefore, the spatial extent of the reaction-diffusion process proceeds with a diffusion limit and at each interval in reaction time the local reaction occurs to high extents (in the absence of a trapping rate). This spatial progression was observed by the persistent diffusion-limited transport of a sharp reaction front as shown in Figure 7a. The limit of $k_p/D\Lambda < 1$ shows that diffusion occurs rapidly; therefore, the reaction-diffusion process exhibits a reaction-limited control of the shape as diffusion is unbounded and extents of reaction are low as shown in Figure 7c. The presence of the photoacid trapping rate, however, changes the
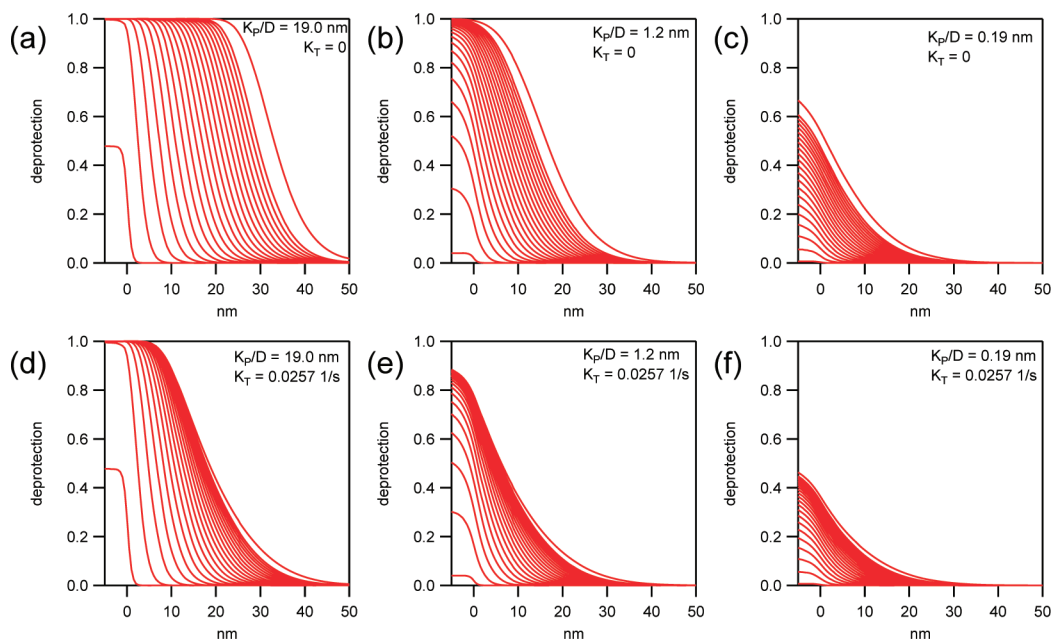


**Figure 7.** Mean-field reaction diffusion model results for deprotection profiles using a fixed $D = 0.525$ nm$^2$/s. (a−c) Profiles in the absence of the trapping constant ($k_T$) at different ratios of $k_P/D$ defined by $k_P = 10$, 0.632, and 0.10 nm$^{-3}$ for a−c, respectively. (d−f) Fixed $k_T = 0.0257$ s$^{-1}$ at varied $k_P/D$.
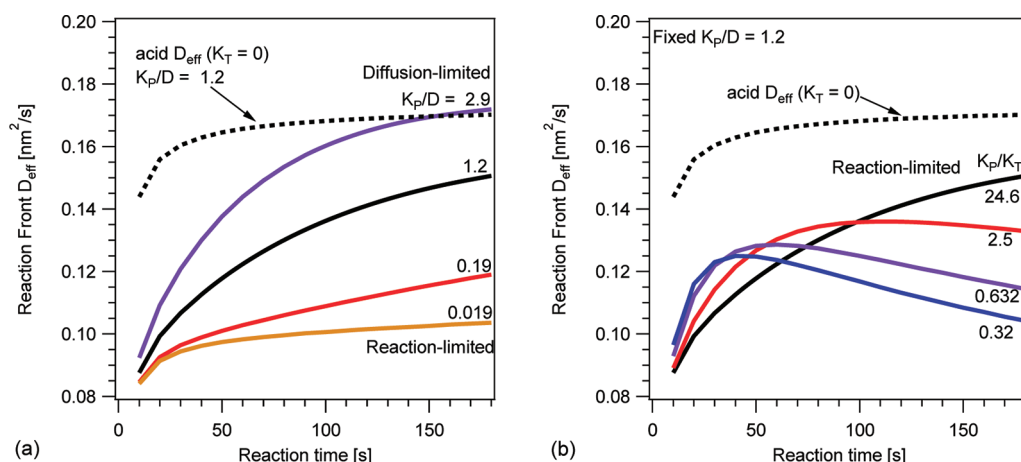
**Figure 8.** Analysis of modeled reaction front profiles in the effective reaction front diffusion as a function of reaction time: (a) $k_P/D$ with fixed $D = 0.525$ nm$^2$/s; (b) fixed $k_P/D = 1.2$ nm and $k_P = 0.632$ nm$^3$/s and increasing values of $k_T$. The calculated effective photoacid diffusion is shown (···) as a diffusion-limited case.

progression of the reaction front as the deprotection profiles converge and become pinned at long reaction times, yet the ratio of $k_P/D$ (with units of nm) remains crucial to achieving a high extent of reaction, which is necessary for imaging, as shown in Figure 7d.

To compare to Figure 6, theoretical $D_{eff}$ values were calculated using $D_{eff} = (L_d)^2/(4t_{PEB})$ from these modeled deprotection fronts in the same manner as the experimental data. The calculated $D_{eff}$ trends predicted by the model equations are shown in Figure 8a and describe the effect of $k_P/D$ above and below 1.2 nm (0.632 nm$^3$s$^{-1}$/0.525 nm$^2$s$^{-1}$) with fixed $k_T = 0.0257$ 1/s. $D_{eff}$ increases and plateaus within reaction times <200 s but is systematically reduced as $k_P/D$ decreases from $k_P/D = 2.9$ nm to a strongly reaction-limited value such as 0.019 nm. The $D_{eff}$ calculated from the photoacid profiles would be a diffusion-limited value shown as the dotted line in the absence of photoacid trapping. Therefore, these materials are more reaction-limited in the spatial progression of the reaction front because the model is below the diffusion limit. Furthermore, Figure 8b shows the effect of the ratio of $k_P/k_T$, where the experimental estimates for d-tBoc-CM4R parameters are $k_P/k_T = 24.6$ (with units nm$^3$), by increasing the trapping constant such that $k_P/k_T$ decreases to 0.32 where a peak in the effective diffusion of the reaction front is observed. This behavior occurs because of the nonlinear reaction diffusion equations with trapping term. Without the trapping term or with a small trapping term, there is no peak in the effective transport as seen in Figure 8b. These model calculations provide insight into the experimental data of Figure 6. Returning to the experimental data, we find that the solid line in Figure 6 is the calculated $D_{eff}$ using the experimental parameters ($k_P = 0.632$ nm$^3$/s, $k_T = 0.0257$ s$^{-1}$, and $D = 0.525$ nm$^2$/s) in the model. The model describes the long-time behavior without any adjustment. Importantly, we used the same approach to extract $L_d$ and calculate $D_{eff}$. However, the experimental peak in $D_{eff}$ is not captured with this set of parameters but it is achievable and conceivable within a range of $k_P/k_T$.

Therefore, deviations in $D_{eff}$ at short reaction times, although possibly caused by experimental artifacts, are consistent with a nonconstant ratio of $k_P/k_T$ with a reaction time that reaches a long-time (or steady-state for autocatalytic reaction fronts) limit. Any attempts to fit would be overparametrization by the

mean-field model and would not carry any quantitative significance. The agreement between the model $D_{eff}$ and the experimental data at long times assures us of the bilayer experimental strategy and the extraction of critical parameters $L_d$ and LILS. These calculations provided a qualitative explanation of the experiment from the model (Figure 6). Furthermore, mean-field models cannot describe the nanometer-level heterogeneous structure induced by the deprotection[51−53] as well as that occurring in model glass formers.[54] The physics of the reaction-diffusion process involves the transport of a small molecule in locally heterogeneously protected and deprotected media. Therefore, photoacid transport depends on the level of deprotection that changes with time. Houle et al. found disparate diffusion coefficients of PFBS (the same photoacid used in this study) in poly-(hydroxystyrene) (PHOST) and t-Boc-protected PHOST,[8] which are the polymer analogues to CM4R and d-t-Boc-CM4R. The PFBS diffusion was nearly 2 orders of magnitude slower in PHOST. The empirical mean-field model used here was developed to treat such heterogeneity caused by reduced transport in deprotected rich regions by the photoacid trapping process.[19,25,55] Short reaction times and low extents of reaction, when the heterogeneity is largest,[52] illustrate why the mean-field model with constant parameters may not capture the experimental trends in $D_{eff}$ at short reaction times. A second fact is the kinetic parameters, determined experimentally, averaged over long reaction times (>90 s). Therefore, the specific application of the bilayer method to shorter times requires considerable attention to reduce sources of systematic error with regard to the initial bilayer interface, initial condition of the PAG, and thermal ramp effects.

**4.3. Comparison to the Mean-Field Reaction−Diffusion Model.** The effective diffusion (Figure 6) can be further tested by comparing the d-t-Boc-CM4R protection spatial extent and shape to the reaction diffusion model calculations. To simplify the comparison, the nonuniformity at the air/film surface was excluded from the fits (and adjusted to match the bulk), therefore considering only the bulk top layer and the reaction front in the bottom layer. Second, the nonuniform substrate layer was adjusted to the fully protected value to facilitate modeling and maintain the experimental bottom film thickness. Lastly, the d-tBoc-CM4R volume fraction profiles were adjusted for volume loss using the known thickness

change as a function of the extent of deprotection. The initial photoacid concentration was fixed to 0.065 acids/nm$^3$, which is the value used in all modeling of the reaction kinetics. Figure 9
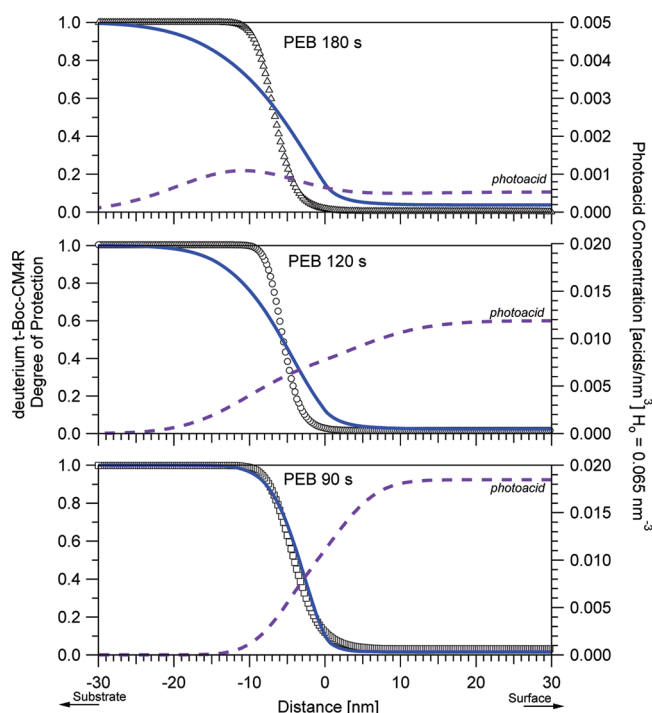


**Figure 9.** Degree of tBoc-CMR protection experimental data (symbols) fit by the reaction-diffusion model deprotection (—) and acid concentration (---) profiles for the positive tone at three PEB times noted. The surface of the low-reactivity substrate layer was not considered by the model. An initial acid concentration of 0.065 acid/nm$^3$ was used, and minimizing the least-squares statistics led to the following parameters: PEB 90 s ($D$ = 0.5250 nm$^2$/s, $k_P$ = 1.1559 nm$^3$/s, $k_T$ = 0.0168 1/s, with $\chi^2$ = 0.1643), PEB 120 s ($D$ = 0.3383 nm$^2$/s, $k_P$ = 0.8813 nm$^3$/s, $k_T$ = 0.0171 1/s with $\chi^2$ = 1.1), and PEB 180 s ($D$ = 0.350 nm$^2$/s, $k_P$ = 1.088 nm$^3$/s, $k_T$ = 0.0304 1/s with $\chi^2$ = 2.88).

shows the experimental data (open symbols) for the longest three PEB times from positive-tone kinetics with the deuterium tBoc-CM4R degree of protection (scaled from 0 to 1) plotted versus distance with the bilayer interface set at the origin (= 0).

The least-squares-minimized nonlinear model fits to the experimental profiles are shown as the solid lines. The overall spatial extent of the model are representative of the experimental data. The results for 90 s are in excellent agreement with systematic deviations at longer times. Deviations in the shape of the extent of reaction above and below the midpoint of the model (protection levels 0.5 to 0.6) are observed. Generally, the model reaction front is broader than the experimental data. This observation shows that the mean-field method appears to capture the average position (spatial extent) of the moving profile but does not capture the nanometer-level shape (profile width).

Because the interfacial widths determined by experiment are narrower than those determined by the model, the initial condition of the photoacid concentration profile is not consistent with a diffuse (nonstep) profile, such as that caused by PAG interdiffusion during sample preparation. Rather, the further narrowing of the interfacial width with PEB time is attributable to an ordering process during the reaction. Molecular resists are able to rearrange cooperatively as the

reaction proceeds, with the reduced interfacial width via the thermodynamic driving force similar to the interfacial width of immiscible or partially miscible polymer blends. Therefore, an annealing process may take place in situ that may not be possible with polymers below the nominal $T_g$ because of topological constraints. Even though processing (80 °C) takes place below the nominal glass transition, the in situ generation and release of gases (deutero-isobutene and $CO_2$, Figure 1) may provide plasticization. The average values of the kinetic parameters are $D$ = (0.40 ± 0.1) nm$^2$/s, $k_P$ = (1.0 ± 0.1) nm$^3$/s, and $k_T$ = (0.021 ± 0.0085) s$^{-1}$, and ratios $k_P/D$ = 2.6 ± 0.4 nm and $k_P/k_T$ = 52 ± 16 nm$^3$ are compared to those determined independently by infrared spectroscopy.[19] The mean-field equations, as shown previously, are sensitive to the ratios $k_P/D$ and $k_P/k_T$ that are within expectations for the fits to the neutron results.

Finally, the predicted effective photoacid concentrations (dashed line) are shown on the right ordinate for each plot. The shape is not always monotonic because of the coupling of the acid concentration to the extent of deprotection via the trapping term (eq 2). The photoacid trapping process causes a peak in the acid concentration in a time- and space-dependent manner within a PEB of 180 s. In the bulk of the film, the photoacid concentration was reduced from the initial level (0.065 acids/nm$^3$) by the trapping process, as expected. These predictions in the acid concentration could be tested by fluorescence lifetime methods that are sensitive to the spatial position (transport) of the photoacid and its acidity (trapping level).[56] It would be important to compare these experimental results to sophisticated stochastic modeling within the reaction and diffusion parameter ranges guided by this work. First principles methods of evaluating and testing resist models are developed by the semiconductor industry[8,10,22,23,57−60] but lack the detailed materials constants and concentration profiles provided by neutron reflectivity experiments.

**4.4. Interfacial Structure of the Developed Image.** Molecular resists do not have entanglements or long chain relaxations; however, dissolution rates do depend upon the average film composition as shown by quartz crystal microbalance studies of blended fractions of protected and unprotected molecular resists.[61,62] Although the kinetics of dissolution cannot be measured by neutron reflectivity, the local structure was probed after the latent image was developed and dried. Upon comparison of the latent and 0.26 mol/L TMAH positive-tone developed images (Figure 4), the CM4R with high degrees of deprotection dissolve (tBoc-rich remain undissolved). The intersection of the developed SLD profile and latent image corresponds to an average SLD such that molecular resist with less than ~6 tBoc-protected CM4Rs dissolve. In polymer photoresists, TMAH development was shown to swell the compositional gradient of the latent image.[63−65] The extent of this residual swelling fraction was confined between the tail of the reaction front and the point where the developed profile intersects the latent image as outlined by the boxed area within the SLD profiles (Figure 4). For PEB times of 120 and 180 s, this zone is ~2 nm; only the 60 s PEB time shows a larger 6-nm-thick zone. In this case, the developed profile must retain the highest tBoc-substituted CM4R as between 46 and 48 nm as the average level of deprotection increased. This can be caused by selective dissolution and deposition when the latent image is more diffuse. Such a mechanism of development within a thin layer may appear via reactive dissolution with a gel layer[66,67] or

perhaps a percolative mechanism.[68] As the latent image sharpens at 120 and 180 s, this zone is eliminated and is on the order of the molecular resist size. The surface roughness quantified by the error function width remained low at 2.5, 2.7, and 2.4 nm for the longest PEB times of 90, 120, and 180 s. Even though the local slope of the composition gradient increases, after development, roughness persists. In this case, additives such as photodegradable bases and amine quenching agents were not required to achieve such low surface roughness[14] as in polymer resists. Therefore, molecular resists define a sharp latent image that in turn minimizes the residual swelling fraction.

Negative-tone development with hexane follows a physical dissolution mechanism, rather than positive-tone development with aqueous hydroxide developers.[66,67,69] In this case, it is the solvent quality that causes dissolution, not the ionization of the weakly acidic hydroxyl groups by titration with the strong base (TMAH). Hexane dissolves d-tBoc-CM4R, but the developed profiles show that low d-tBoc-substituted CM4R must remain. Therefore, the hexane dissolved the tBoc-protected CM4R in a selective manner throughout the deprotection profile (Figure 5). Figure 5 for the PEB of 60 s illustrates the zone between the tail of the reaction front at 16 nm and the midpoint of the developed image at 26 nm, highlighted by the dotted−dashed box, which shows a lower SLD (protection level) than the latent image profile. Hexane must enter the reaction front to permit a sieving of d-tBoc-CM4R from this interphase. This appears more as a percolative development, such as that developed for novolak resists,[68] but via organic solvent and without the ionization of the phenolic groups (reactive development[66,67]). Subsequently, during drying, the remaining deprotected CM4R leaves a dense layer with surface roughness. Therefore, the residual swelling fraction depends upon the tone of development for molecular resists. The thickness of this zone is 9.8, 9.2, and 8.5 nm for 60, 120, and 180 s PEB times and is larger than the molecular resist size. A consequence of this larger residual swelling fraction is a larger surface roughness; 4.2, 3.3, 3.3, and 3.0 nm for PEB times of 30, 60, 120, and 180 s.

The spatial extent of this rearranging fraction is a resolution limit. For a line-space feature on the order of this length scale, one would not expect any feature with high fidelity. This depends upon the tone of development, and positive tone predicts a smaller printable feature than negative tone with the same molecular resist. Furthermore, the latent image slope, near the average composition of solubility, between positive tone and negative tone was similar in magnitude (Table 1), with the negative-tone slope being slightly smaller at long PEB times. The lower LILS correlates with larger roughness, yet the developed roughness appears to follow alternate development mechanisms involving a restructuring. Statistical-resolution-limit models as described by eq 1 do not consider the dissolution in the presence of the underlying latent image composition profile.

## 5. CONCLUSIONS

Neutron reflectivity measurements on model lithographic line edges show that the characteristic lengths of the reaction front exceed molecular resist dimensions because of photoacid diffusion. A common photoacid leads to an effective diffusion of the reaction front consistent with reaction-limited transport. A mean-field reaction-diffusion model with an empirical photoacid-trapping term restricts the spatial progression of

photoacid and captures the spatial extent. However, the local shape does not match the experimental data well at long reaction times. Such mean-field models cannot consider the local heterogeneous structure that forms because of chemical reactions. This effect may appear to be a nonconstant ratio of the reaction rate to the trapping rate. The various protecting groups available with different polarities provide a chemical handle to modify such behavior experimentally.

Latent image and development control cannot be treated separately in designing next-generation resist materials, whether chemically amplified or nonchemically amplified. This is because a thin zone of resist that is capable of restructuring during development appears even with molecular resists. The concept of a residual swelling fraction, observed for polymers, holds for d-tBoc-CM4R negative-tone solvent development. Positive-tone aqueous base development exhibits no residual swelling fraction after reaction times longer than 60 s. The ability of tBoc-CM4R to achieve a large deprotection slope reduces the interpenetration and rearrangement of partially protected tBoc-CM4R with TMAH. This is an advantage over polymer resists that readily swell. Additives used in development to reduce LER presumably adsorb or induce surface rearrangement. These neutron reflectivity data provide a hypothesis to understand these mechanisms. As evidence, partially protected CM4R rearranges at the feature edge during negative-tone development, causing an enrichment of deuterated tBoc groups on the surface. The final roughness also plateaus but remains low even at image log slopes higher than achieved with photolithography. Therefore, even though these molecular resists with high-activation-energy protecting groups, such as tBoc, require high reaction temperatures, photoacid diffusion may not limit their applicability but rather induce development mechanisms that resembles "pixel" rearrangement.

In perspective, molecular resists such as calix[4]-resorcinarenes provide an advantage in addition to their smaller size. Their phase behavior can be controlled to introduce microphase separation and even crystallization as a chemical handle to improve image fidelity. In the present case, the purified, protected all-cis isomer cannot undergo conformation rearrangement and may crystallize. These spin-cast films do not exhibit bulk crystallinity and therefore are supercooled, and upon deprotection, the ring may invert, giving a distribution of cis and trans isomers and stabilizing the noncrystalline amorphous state. The methyl substitution of the CM4R provides a handle for controlling phase behavior and providing a more polar structure to introduce microphase separation.[70−73] The present work that stimulates the combination of chemical amplification with disorder-to-order transitions at the developing resist interface may provide self-healing material. For instance, the narrowing of the reaction front width, when compared to the mean-field model, is suggestive of mechanisms that reduce the interfacial width. Combining molecular resists with low-activation-energy protecting groups would avoid elevated temperatures and favor low photoacid diffusion as observed by Wallraff et al. with ketal- or acetal-protected poly(hydroxystyrene).[74] Such similar molecular resist materials would test mechanisms regarding the temperature dependence of interfacial width broadened by photoacid diffusion versus those sharpened by rearrangement during the reaction.

## ■ ASSOCIATED CONTENT

### ⓢ Supporting Information

Reflectivity of the positive-tone samples for latent and developed images. Reflectivity of the negative-tone samples for latent and hexane developed images. Neutron and X-ray reflectivity on the same sample. This material is available free of charge via the Internet at http://pubs.acs.org.

## ■ AUTHOR INFORMATION

### Corresponding Author

*E-mail: vprabhu@nist.gov. Tel: 1-301-975-3657.

### Notes

The authors declare no competing financial interest.

## ■ ACKNOWLEDGMENTS

## ■ REFERENCES

(1) Ito, H.; Willson, C. G. Chemical amplification in the design of dry developing resist materials. *Polym. Eng. Sci.* **1983**, 23, 1012−1018.

(2) Ito, H. Chemical amplification resists for microlithography. *Adv. Polym. Sci.* **2005**, 172, 37−245.

(3) International Technology Roadmap for Semiconductors, 2009 ed;. http://www.itrs.net 2009, lithography section, p 9.

(4) Hinsberg, W.; Houle, F. A.; Hoffnagle, J.; Sanchez, M.; Wallraff, G.; Morrison, M.; Frank, S. Deep-ultraviolet interferometric lithography as a tool for assessment of chemically amplified photoresist performance. *J. Vac. Sci. Technol., B* **1998**, 16, 3689−3694.

(5) Hinsberg, W. D.; Houle, F. A.; Sanchez, M.; Morrison, M.; Wallraff, G. M.; Larson, C.; Hoffnagle, J.; Brock, P.; Breyta, G. Effect of resist components on image spreading during postexposure bake of chemically amplified resists. *Proc. SPIE* **2000**, 3999, 148.

(6) Pawloski, A.; Acheta, A.; Lalovic, I.; LaFontaine, B.; Levinson, H. Characterization of line edge roughness in photoresist using an image fading technique. *Proc. SPIE* **2004**, 5376, 414.

(7) Hinsberg, W. D.; Houle, F. A.; Sanchez, M. I.; Wallraff, G. M. Chemical and physical aspects of the post-exposure baking process used for positive-tone chemically amplified resists. *IBM J. Res. Dev.* **2001**, 45, 667−682.

(8) Houle, F. A.; Hinsberg, W. D.; Morrison, M.; Sanchez, M. I.; Wallraff, G.; Larson, C.; Hoffnagle, J. Determination of coupled acid catalysis-diffusion processes in a positive-tone chemically amplified photoresist. *J. Vac. Sci. Technol., B* **2000**, 18, 1874−1885.

(9) Houle, F. A.; Hinsberg, W. D.; Sanchez, M. I.; Hoffnagle, J. A. Influence of resist components on image blur in a patterned positive-tone chemically amplified photoresist. *J. Vac. Sci. Technol., B* **2002**, 20, 924−931.

(10) Houle, F. A.; Hinsberg, W. D.; Sanchez, M. I. Acid-base reactions in a positive tone chemically amplified photoresist and their effect on imaging. *J. Vac. Sci. Technol., B* **2004**, 22, 747−757.

(11) Lin, E. K.; Soles, C. L.; Goldfarb, D. L.; Trinque, B. C.; Burns, S. D.; Jones, R. L.; Lenhart, J. L.; Angelopoulos, M.; Willson, C. G.; Satija, S. K.; Wu, W. L. Direct measurement of the reaction front in chemically amplified photoresists. *Science* **2002**, 297, 372−375.

(12) Goldfarb, D. L.; Angelopoulos, M.; Lin, E. K.; Jones, R. L.; Soles, C. L.; Lenhart, J. L.; Wu, W. L. Confinement effects on the spatial extent of the reaction front in ultrathin chemically amplified photoresists. *J. Vac. Sci. Technol., B* **2001**, 19, 2699−2704.

(13) Vogt, B. D.; Kang, S.; Prabhu, V. M.; Lin, E. K.; Satija, S. K.; Turnquest, K.; Wu, W. Measurements of the reaction-diffusion front of model chemically amplified photoresists with varying photoacid size. *Macromolecules* **2006**, 39, 8311−8317.

(14) Vogt, B. D.; Kang, S.; Prabhu, V. M.; Rao, A.; Lin, E. K.; Wu, W. L.; Satija, S. K.; Turnquest, K. Influence of base additives on the reaction diffusion front of model chemically amplified photoresists. *J. Vac. Sci. Technol., B* **2006**, 25, 175−182.

(15) Lavery, K. A.; Vogt, B. D.; Prabhu, V. M.; Lin, E. K.; Wu, W. L.; Satija, S. K.; Choi, K. W. Exposure dose effects on the reaction-diffusion process in model extreme ultraviolet photoresists. *J. Vac. Sci. Technol., B* **2006**, 24, 3044−3047.

(16) Prabhu, V. M.; Kang, S. H.; VanderHart, D. L.; Satija, S. K.; Lin, E. K.; Wu, W. L. Photoresist latent and developer images as probed by neutron reflectivity methods. *Adv. Mater.* **2011**, 23, 388−408.

(17) VanderHart, D. L.; Prabhu, V. M.; Lin, E. K. Proton NMR determination of miscibility in a bulk model photoresist system: Poly(4-hydroxystyrene) and the photoacid generator, di(tert-butylphenyl)iodonium perfluorooctanesulfonate. *Chem. Mater.* **2004**, 16, 3074−3084.

(18) VanderHart, D. L.; Prabhu, V. M.; De Silva, A.; Felix, N. M.; Ober, C. K. Solid state NMR investigation of photoresist molecular glasses including blend behavior with a photoacid generator. *J. Mater. Chem.* **2009**, 19, 2683−2694.

(19) Kang, S. H.; Wu, W. L.; Choi, K. W.; De Silva, A.; Ober, C. K.; Prabhu, V. M. Characterization of the photoacid diffusion length and reaction kinetics in EUV photoresists with IR spectroscopy. *Macromolecules* **2010**, 43, 4275−4286.

(20) Kozawa, T.; Tagawa, S.; Santillan, J. J.; Toriumi, M.; Itani, T. Image contrast slope and line edge roughness of chemically amplified resists for postoptical lithography. *J. Vac. Sci. Technol., B* **2007**, 25, 2295−2300.

(21) Erdmann, A.; Fuhner, T.; Shao, F.; Evanschitzky, P. Lithography simulation: modeling techniques and selected applications. *Proc. SPIE* **2009**, 7390, 739002.

(22) Rathsack, B.; Nafus, K.; Hatakeyama, S.; Kuwahara, Y.; Kitano, J.; Gronheid, R.; Pret, A. V. Resist fundamentals for resolution, LER, and sensitivity (RLS) performance tradeoffs and their relation to micro-bridging defects. *Proc. SPIE* **2009**, 7273, 727347-11.

(23) Robertson, S. A.; Biafore, J. J.; Smith, M. D.; Reilly, M. T.; Wandell, J. Stochastic simulation of resist linewidth roughness and critical dimension uniformity for optical lithography. *J. Micro/Nanolithogr., MEMS, MOEMS* **2010**, 9, 041212.

(24) Mack, C. A. Stochastic modeling in lithography: autocorrelation behavior of catalytic reaction-diffusion systems. *J. Micro/Nanolithogr., MEMS, MOEMS* **2009**, 8, 029701.

(25) Sha, J.; Lee, J. K.; Kang, S. H.; Prabhu, V. M.; Soles, C. L.; Bonnesen, P. V.; Ober, C. K. Architectural effects on acid reaction-diffusion kinetics in molecular glass photoresists. *Chem. Mater.* **2010**, 22, 3093−3098.

(26) Bekaert, J.; Van Look, L.; Truffert, V.; Lazzarino, F.; Vandenberghe, G.; Reybrouck, M.; Tarutani, S. Comparing positive and negative tone development process for printing the metal and contact layers of the 32-and 22-nm nodes. *J. Micro/Nanolithogr., MEMS, MOEMS* **2010**, 9, 043007.

(27) Tarutani, S.; Tsubaki, H.; Kanna, S. Development of materials and processes for double patterning toward 32 nm node ArF immersion lithography. *J. Photopolym. Sci. Technol.* **2008**, 21, 685−690.

(28) Cram, D. J.; Karbach, S.; Kim, H. E.; Knobler, C. B.; Maverick, E. F.; Ericson, J. L.; Helgeson, R. C. Host guest complexation 0.46. Cavitands as open molecular vessels form solvates. *J. Am. Chem. Soc.* **1988**, *110*, 2229−2237.

(29) Ito, H.; Nakayama, T.; Sherwood, M.; Miller, D.; Ueda, M. Characterization and lithographic application of calix[4]resorcinarene derivatives. *Chem. Mater.* **2008**, *20*, 341−356.

(30) Wei, I. Y. Syntheses of 2-chloro-2-methylpropane-1,1,1,3,3,3-D6, 2-chloro-2-methylpropane-D9, 2,2-dimethyl-D6-propane-1,1,1-D3 and 2,2-dimethyl-propane-D12. *J. Labelled Compd.* **1974**, *10*, 355−359.

(31) Pope, B. M.; Yamamoto, Y.; Tarbell, D. S. Di-tert-butyl Dicarbonate. *Org. Synth.* **1988**, *50−9*, 418−421.

(32) Kurian, A.; Prasad, S.; Dhinojwala, A. Unusual surface aging of poly(dimethylsiloxane) elastomers. *Macromolecules* **2010**, *43*, 2438−2443.

(33) Kienzle, P.; O'Donovan, K.; Ankner, J.; Berk, N.; Majkrzak, C. NCNR Reflectometry Software. http://www.ncnr.nist.gov/reflpak 2006.

(34) Bevington, P. R. *Data Reduction and Error Analysis for the Physical Sciences*; McGraw-Hill: New York, 1969.

(35) Kang, S. H.; Prabhu, V. M.; Soles, C. L.; Lin, E. K.; Wu, W. L. Methodology for quantitative measurements of multilayer polymer thin films with IR spectroscopic ellipsometry. *Macromolecules* **2009**, *42*, 5296−5302.

(36) Prabhu, V. M.; Kang, S. H.; Kline, R. J.; DeLongchamp, D. M.; Fischer, D. A.; Wu, W. L.; Satija, S. K.; Bonnesen, P. V.; Sha, J.; Ober, C. K. Characterization of the non-uniform reaction in chemically amplified calix[4]resorcinarene molecular resist thin films. *Aust. J. Chem.* **2011**, *64*, 1065−1073.

(37) Hinsberg, W. D.; Macdonald, S. A.; Clecak, N. J.; Snyder, C. D. Airborne contamination of a chemically amplified resist 0.2. Effect of polymer film properties on contamination rate. *Chem. Mater.* **1994**, *6*, 481−488.

(38) Lenhart, J. L.; Jones, R. L.; Lin, E. K.; Soles, C. L.; Wu, W. L.; Fischer, D. A.; Sambasivan, S.; Goldfarb, D. L.; Angelopoulos, M. Probing surface and bulk chemistry in resist films using near edge X-ray absorption fine structure. *J. Vac. Sci. Technol., B* **2002**, *20*, 2920−2926.

(39) Lenhart, J. L.; Fischer, D. A.; Sambasivan, S.; Lin, E. K.; Jones, R. L.; Soles, C. L.; Wu, W. L.; Goldfarb, D. L.; Angelopoulos, M. X-ray absorption spectroscopy to probe surface composition and surface deprotection in photoresist films. *Langmuir* **2005**, *21*, 4007−4015.

(40) Yim, H.; Kent, M.; McNamara, W. F.; Ivkov, R.; Satija, S.; Majewski, J. Structure within thin epoxy films revealed by solvent swelling: a neutron reflectivity study. *Macromolecules* **1999**, *32*, 7932−7938.

(41) Prabhu, V. M.; Sambasivan, S.; Fischer, D.; Sundberg, L. K.; Allen, R. D. Quantitative depth profiling of photoacid generators in photoresist materials by near-edge X-ray absorption fine structure spectroscopy. *Appl. Surf. Sci.* **2006**, *253*, 1010−1014.

(42) Fukushima, Y.; Watanabe, T.; Ohnishi, R.; Shiotani, H.; Suzuki, S.; Hayakawa, M.; Endo, Y.; Yamanaka, T.; Yusa, S.; Kinoshita, H. Optimization of photoacid generator in photoacid generation-bonded resist. *Jpn. J. Appl. Phys.* **2008**, *47*, 6293−6296.

(43) Wang, M. X.; Gonsalves, K. E.; Rabinovich, M.; Yueh, W.; Roberts, J. M. Novel anionic photoacid generators (PAGs) and corresponding PAG bound polymers for sub-50 nm EUV lithography. *J. Mater. Chem.* **2007**, *17*, 1699−1706.

(44) Wang, M. X.; Lee, C. T.; Henderson, C. L.; Yueh, W.; Roberts, J. M.; Gonsalves, K. E. Incorporation of ionic photoacid generator (PAG) and base quencher into the resist polymer main chain for sub-50 nm resolution patterning. *J. Mater. Chem.* **2008**, *18*, 2704−2708.

(45) Wu, H. P.; Gonsalves, K. E. Preparation of a photoacid generating monomer and its application in lithography. *Adv. Funct. Mater.* **2001**, *11*, 271−276.

(46) Brainard, R.; Hassanein, E.; Li, J.; Pathak, P.; Thiel, B.; Cerrina, F.; Moore, R.; Rodriguez, M.; Yakshinskiy, B.; Loginova, E.; Madey, T.; Matyi, R.; Malloy, M.; Rudack, A.; Naulleau, P.; Wuest, A.; Dean, K. Photons, electrons, and acid yields in EUV photoresists: a progress report. Henderson, C. L., Ed.; SPIE: San Jose, CA, 2008; p 692325-14.

(47) Bristol, R. L. The tri-lateral challenge of resolution, photospeed, and LER: scaling below 50nm? Lin, Q., Ed.; Proceedings of SPIE: San Jose, CA, 2007; pp 65190W−651911.

(48) Gallatin, G. M.; Naulleau, P.; Niakoula, D.; Brainard, R.; Hassanein, E.; Matyi, R.; Thackeray, J.; Spear, K.; Dean, K. Resolution, LER, and sensitivity limitations of photoresists. Schellenberg, F. M., Ed.; Proceedings of SPIE: San Jose, CA, 2008; pp 69211E-11.

(49) Van Steenwinckel, D.; Gronheid, R.; Lammers, J. H.; Meyers, A. M.; Van Roey, F.; Willems, P. A novel method for characterizing resist performance. Lin, Q., Ed.; Proceedings of SPIE: San Jose, CA, 2007; pp 65190V−651911.

(50) Probstein, R. F. *Physicochemical Hydrodynamics*; 2nd ed.; John Wiley & Sons: New York, 1994.

(51) Jones, R. L.; Hu, T. J.; Lin, E. K.; Wu, W. L.; Goldfarb, D. L.; Angelopoulos, M.; Trinque, B. C.; Schmid, G. M.; Stewart, M. D.; Willson, C. G. Formation of deprotected fuzzy blobs in chemically amplified resists. *J. Polym. Sci., Part B: Polym. Phys.* **2004**, *42*, 3063−3069.

(52) Kang, S.; Vogt, B. D.; Wu, W. L.; Prabhu, V. M.; VanderHart, D. L.; Rao, A.; Lin, E. K.; Turnquest, K. Characterization of compositional heterogeneity in chemically amplified photoresist polymer thin films with infrared spectroscopy. *Macromolecules* **2007**, *40*, 1497−1503.

(53) Rao, A.; Kang, S.; Vogt, B. D.; Prabhu, V. M.; Lin, E. K.; Wu, W. L.; Muthukumar, M. Effect of deprotection extent on swelling and dissolution regimes of thin polymer films. *Langmuir* **2006**, *22*, 10009−10015.

(54) Ediger, M. D. Spatially heterogeneous dynamics in supercooled liquids. *Annu. Rev. Phys. Chem.* **2000**, *51*, 99−128.

(55) Kang, S.; Prabhu, V. M.; Vogt, B. D.; Lin, E. K.; Wu, W. l.; Turnquest, K. Effect of copolymer composition on acid-catalyzed deprotection reaction kinetics in model photoresists. *Polymer* **2006**, *47*, 6293−6302.

(56) Vallee, R. A. L.; Paul, W.; Binder, K. Single molecule probing of the glass transition phenomenon: simulations of several types of probes. *J. Chem. Phys.* **2007**, *127*, 154903.

(57) Biafore, J. J.; Smith, M. D.; van Setten, E.; Wallow, T.; Naulleau, P.; Blankenship, D.; Robertson, S. A.; Deng, Y. F. Resist pattern prediction at EUV. *Proc. SPIE* **2010**, *7636*, 76360R-1−76360R-10.

(58) Robertson, S. A.; Biafore, J. J.; Smith, M. D.; Reilly, M. T.; Wandell, J. Predictive linewidth roughness and CDU simulation using a calibrated physical stochastic resist model. *Proc. SPIE* **2010**, *7639*, 763934.

(59) Smith, M. D.; Byers, J. D.; Mack, C. A. The lithographic impact of resist model parameters. *Proc. SPIE* **2004**, *5376*, 322−332.

(60) Smith, M. D.; Mack, C. A. Process sensitivity and optimization with full and simplified resist models. *Proc. SPIE* **2003**, *5040*, 1509−1520.

(61) De Silva, A.; Sundberg, L. K.; Ito, H.; Sooriyakumaran, R.; Allen, R. D.; Ober, C. K. A fundamental study on dissolution behavior of high-resolution molecular glass photoresists. *Chem. Mater.* **2008**, *20*, 7292−7300.

(62) Toriumi, M.; Santillan, J.; Itani, T.; Kozawa, T.; Tagawa, S. Dissolution characteristics and reaction kinetics of molecular resists for extreme-ultraviolet lithography. *J. Vac. Sci. Technol., B* **2007**, *25*, 2486−2489.

(63) Prabhu, V. M.; Vogt, B. D.; Kang, S.; Rao, A.; Lin, E. K.; Satija, S. K. Direct measurement of the spatial extent of the in situ developed latent image by neutron reflectivity. *J. Vac. Sci. Technol., B* **2007**, *25*, 2514−2520.

(64) Prabhu, V. M.; Vogt, B. D.; Kang, S.; Rao, A.; Lin, E. K.; Satija, S. K.; Turnquest, K. Direct measurement of the in situ developed latent image: the residual swelling fraction. *Proc. SPIE* **2007**, *6519*, 651910.

(65) Prabhu, V. M.; Rao, A.; Kang, S.; Lin, E. K.; Satija, S. K. Manipulation of the asymmetric swelling fronts of photoresist

polyelectrolyte gradient thin films. *J. Phys. Chem. B* **2008**, *112*, 15628−15635.

(66) Hinsberg, W.; Houle, F. A.; Lee, S. W.; Ito, H.; Kanazawa, K. Characterization of reactive dissolution and swelling of polymer films using a quartz crystal microbalance and visible and infrared reflectance spectroscopy. *Macromolecules* **2005**, *38*, 1882−1898.

(67) Hinsberg, W. D.; Houle, F. A.; Ito, H. Reactive dissolution oflithographic copolymers. *Proc. SPIE* **2004**, *5376*, 352−359.

(68) Reiser, A.; Shih, H. Y.; Yeh, T. F.; Huang, J. P. Novolak-diazoquinone resists: the imaging systems of the computer chip. *Angew. Chem., Int. Ed. Engl.* **1996**, *35*, 2428−2440.

(69) Houle, F. A.; Hinsberg, W. D.; Sanchez, M. I. Kinetic model for positive tone resist dissolution and roughening. *Macromolecules* **2002**, *35*, 8591−8600.

(70) Shinkai, S. Calixarenes - the 3rd-generation of supramolecules. *Tetrahedron* **1993**, *49*, 8933−8968.

(71) Dalgarno, S. J.; Warren, J. E.; Atwood, J. L.; Raston, C. L. Versatility of p-sulfonatocalix[5] arene in building up multicomponent bilayers. *New J. Chem.* **2008**, *32*, 2100−2107.

(72) Podoprygorina, G.; Janke, M.; Janshoff, A.; Bohmer, V. Self-assembled polymers based on bis-tetra-urea calix[4]arenes connected via the wide rim. *Supramol. Chem.* **2008**, *20*, 59−69.

(73) Baldini, L.; Casnati, A.; Sansone, F.; Ungaro, R. Calixarene-based multivalent ligands. *Chem. Soc. Rev.* **2007**, *36*, 254−266.

(74) Wallraff, G. M.; Medeiros, D. R.; Sanchez, M.; Petrillo, K.; Huang, W. S.; Rettner, C.; Davis, B.; Larson, C. E.; Sundberg, L.; Brock, P. J.; Hinsberg, W. D.; Houle, F. A.; Hoffnagle, J. A.; Goldfarb, D.; Temple, K.; Wind, S.; Bucchignano, J. Sub-50 nm half-pitch imaging,with a low activation energy chemically amplified photoresist. *J. Vac. Sci. Technol., B* **2004**, *22*, 379−3484.